



ÉCOLE POLYTECHNIQUE FÉDÉRALE DE LAUSANNE

Towards replicating the full chewing process: Initial development of a Stewart platform-based chewing robot.

MASTER THESIS

Author:

Barbara DE GROOT, 296815

CREATE Lab, Prof. Josie Hughes
Supervisor: Benhui Dai

June 20, 2025

Contents

1	Introduction	3
2	Methods	4
2.1	Design requirements from human physiology	4
2.2	Mechanical design	4
2.2.1	6-DoF mechanism	4
2.2.2	Actuator requirements and selection	5
2.2.3	Jaw subassemblies	6
2.2.4	Full assembly	7
2.3	Control system	9
2.3.1	Hardware (electronics)	9
2.3.2	Software architecture	10
2.3.3	Stewart platform control	11
2.3.4	Force sensing	13
2.4	Data acquisition and processing	14
2.4.1	Subjects	14
2.4.2	Motion-capture acquisition	14
2.4.3	Data processing	15
3	Results	15
3.1	Motion captured chewing trajectories	15
3.2	Position control	16
3.3	Force analysis	18
3.3.1	Maximum force	18
3.3.2	Force feedback distribution	18
3.4	Scalability and modularity	19
4	Discussion	20
4.1	Summary of Findings	20
4.2	Limitations	20
4.2.1	Mechanical design	20
4.2.2	Electronics and control	20

4.2.3	Motion capture recordings	21
4.3	Future Work	21
4.3.1	Mechanical design improvements	21
4.3.2	Control system improvements	21
5	Conclusion	22
6	References	23
7	Appendix	25
7.1	Real robot pictures	25
7.2	Electronics connections to Teensy 4.1	27

1 Introduction

Oral mastication is a complex process, involving different components such as the jaw, teeth, tongue and saliva, all coordinated to break down food into a bolus that can be swallowed and digested. Chewing robots are a great tool for studying this process, as they give us the opportunity for a closely controlled environment where each parameter can be adjusted and measured. This makes them valuable not only for advancing our understanding of chewing mechanics and related disorders, but also for a wide range of applications. In dentistry, they are used to test how implants and other dental devices wear over time [1]. In food science, they help assess texture [2] and flavor release during mastication. They also offer a reliable platform for studying the release of active compounds in chewable medications such as medical chewing gum [3].

Today, many chewing robots have already made significant progress in mimicking human chewing movements. For example, the Bristol Dento-Munch Robo-Simulator [4] features 6 degrees of freedom (DoF), closed-loop control, force feedback, and a full set of teeth capable of replicating human chewing forces. Similarly, the robot developed by Seung-Ju et al. [5] offers the same capabilities, with a design that matches more closely human biomechanics. Another system, by Alemzadeh et al. [3], includes a closed mouth and artificial saliva—two important components of realistic mastication—even though it has limited sensory feedback. However, no existing system combines all critical elements as fully integrated as humans: 6-DoF, position and multidirectional force feedback, a hermetically closed mouth with saliva circulation, and an actuated tongue. Without them it is not possible to accurately reproduce the entire chewing process. For example, without a tongue, the robot cannot direct the food towards the teeth during chewing or without saliva, the food cannot be mixed with enzymes that aid digestion. This greatly limits what kind of chewing experiments can be performed, as well as the robot’s ability to adapt to different food types and textures.

This project addresses that gap by taking the first step toward an all-inclusive chewing robot. The present work concentrates on the mechanical foundation: a modular 6-DoF Stewart platform-based jaw sized from physiological data, equipped with tri-axial force sensing and position feedback. The overarching research question is therefore narrowed to:

How can a modular Stewart-platform jaw be designed and validated so that it reproduces human chewing trajectories and forces while exposing interfaces for future tongue and saliva modules?

To answer this question, we (i) designed and built the platform matching human anatomy, (ii) implemented a closed-loop system with sensory-motor control, (iii) recorded a motion-capture dataset of human chewing and analyzed it, and (iv) replicated these trajectories on the robot to validate its performance. By laying down a flexible, expandable foundation, this work enables future integration of artificial saliva flow, an artificial tongue and adaptive bio-inspired control, moving one step closer to a robot that replicates the complete human chewing process.

2 Methods

2.1 Design requirements from human physiology

The jaw makes essential contributions to the chewing process such as generating the forces required to break down food, controlling the lower mandible motion and giving sensory feedback. A robotic jaw should therefore be able to mimic these functions as closely as possible. We first focus on force generation and range of motion, to build the structure of the chewing robot. The design requirements are based on the human jaw anatomy and physiology, as summarized in Table 1.

Quantity	Values reported in the literature	Design requirement
DoF	6-DoF: 3 translational (X, Y, Z) and 3 rotational (roll, pitch, yaw) [6]	6-DoF
Vertical (compressive) bite force F_z	600 N chewing force in healthy adults [7], 1243 N maximum clenching force [8]	800 N
Lateral force F_x	-72 N (left) to +53 N (right) during maximal biting [9]	± 100 N
Anterior-posterior force F_y	-10 N (posterior) to +30 N (anterior) [9]	± 50 N
Mandibular motion range	14 mm lateral shift, 11 mm protrusion, 61 mm mouth opening in healthy adults [10]	± 20 mm (X, Y); 0–60 mm (Z)

Table 1: Functional design requirements.

2.2 Mechanical design

This section details the key design decisions that led to the final mechanical design of the chewing robot and the resulting specifications.

2.2.1 6-DoF mechanism

The first major design decision was how to achieve 6-DoF for jaw motion. In the field of robotic mastication, two common approaches are used. The first is a biomechanically inspired design using linear actuators [5] or combinations of actuated cables and springs [3] to replicate muscle behavior. The second is a Stewart platform [4]—a widely used 6-DoF parallel mechanism, often seen in motion simulators. See Figure 1 for a visualization of the two approaches.

For this project, we chose the Stewart platform approach. Its well-defined kinematics and ease of control make it particularly suitable for our goal of replicating recorded human chewing motion. Because our control strategy is based on reproducing real motion trajectories, having a platform with straightforward inverse kinematics is a key advantage.

Stewart platforms generally come in two configurations: one based on rotary servo motors and one based on linear actuators, see Figure 1. We selected the linear actuator design for several reasons. It offers more efficient force transmission, a simpler kinematic model, and greater structural rigidity—all important factors when attempting to reproduce the forces involved in human chewing.

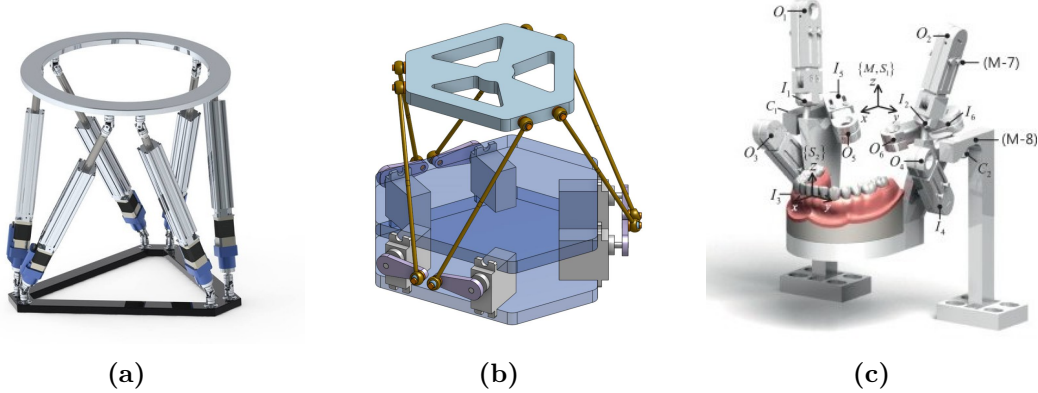


Figure 1: (a) Linear actuator-based Stewart platform. (b) Rotary servo motor-based Stewart platform. (c) Biomechanically inspired robotic jaw design[5].

2.2.2 Actuator requirements and selection

The combination of high bite-force replication and position feedback demands actuators large enough to deliver both power and sensing hardware; their size therefore becomes a critical design constraint. Their stroke and force requirements are fixed by the functional criteria in Table 1.

Design assumptions. To compute the required actuator specifications, we assumed a minimum actuator mounting angle of at least 45° to the horizontal and the general geometry of the platform and base shown in Figure 2.

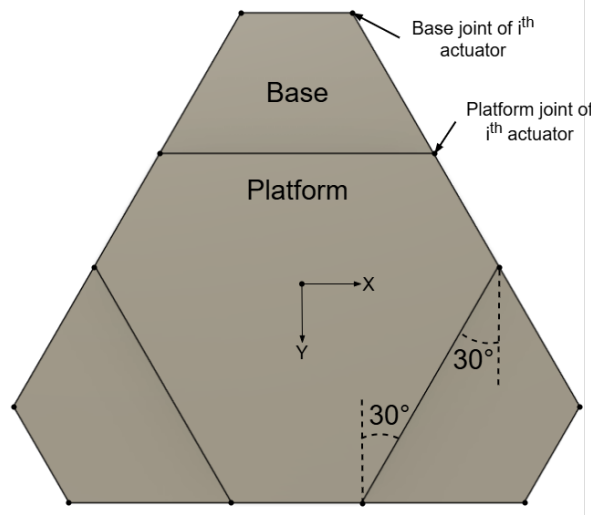


Figure 2: Top view of the base and platform design assumption.

Stroke length. Guided by the workspace analysis from Masory et al. [11], we prioritize achieving the necessary vertical range of motion, knowing that sufficient horizontal range would follow. The minimum required stroke length is:

$$l_{\min} = \frac{z_{\max} - z_{\min}}{\sin(45^\circ)} = \frac{70 \text{ mm}}{\sin(45^\circ)} \approx 99 \text{ mm} \quad (1)$$

Load. To meet the minimum vertical force requirement of 800 N, each actuator must provide a load of at least:

$$F_{\min} = \frac{F_{z,\min}}{6 \cdot \sin(45^\circ)} = \frac{800 \text{ N}}{6 \cdot \sin(45^\circ)} \approx 189 \text{ N} \quad (2)$$

With this minimum actuator force, we estimate the lateral (shear) and front-back force capacities as:

$$F_x \approx 2 \cdot \cos(45^\circ) \cdot F_{\min} + 4 \cdot \cos(45^\circ) \cdot \sin(30^\circ) \cdot F_{\min} \approx 534 \text{ N} \gg 100 \text{ N} \quad (3)$$

$$F_y \approx 4 \cdot \cos(45^\circ) \cdot \cos(30^\circ) \cdot F_{\min} \approx 462 \text{ N} \gg 50 \text{ N} \quad (4)$$

These calculations show that ensuring the vertical force requirement is met also guarantees that shear forces in the x and y directions will exceed their respective targets.

Speed and feedback. Since speed is not a requirement for this prototype, we prioritized force over velocity when selecting actuators. Position feedback is necessary for closed-loop control, as we use inverse kinematics to compute actuators lengths based on the desired platform pose.

Selection. We selected the PA-14P-4-50 linear actuator, which meets both stroke and force requirements as seen in Table 2. The dimensions of both base and platform, see Figure 3, were chosen to accommodate the size of the actuators. The resulting vertical workspace of the platform is 118 mm, which is more than enough to cover the required 70 mm.

At mid-stroke, the actuators are positioned at an angle of 60° relative to the horizontal plane. Under this configuration, the theoretical maximum force outputs are: $F_{z,max} = 1155 \text{ N}$ (vertical), $F_{x,max} = 444 \text{ N}$ (lateral), and $F_{y,max} = 385 \text{ N}$ (anterior-posterior). All values surpass the design requirements specified in Table 1. These are idealized values and do not account for frictional losses or mechanical inefficiencies.

Parameter	Value
Stroke length	101 mm
Max force	222.4 N
Speed (no load)	28 mm/s
Speed (full load)	21 mm/s
Position feedback	Potentiometer
Protection class	IP54
Power supply	12 V DC

Table 2: PA-14P-4-50 specifications.

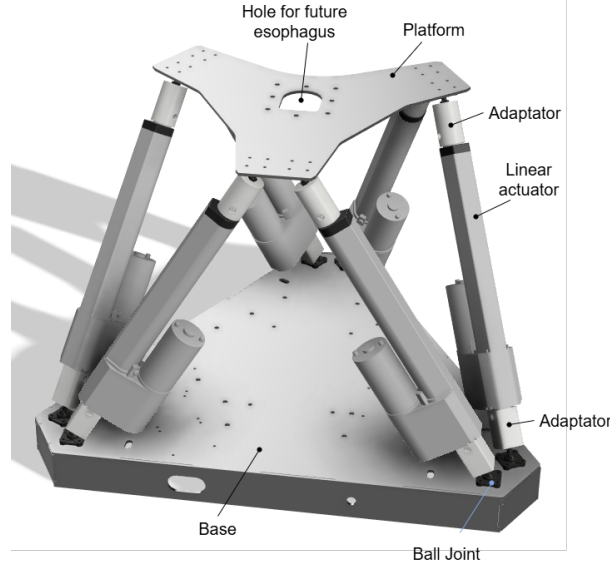


Figure 3: Final Stewart platform design.

2.2.3 Jaw subassemblies

Next, we designed the lower and upper jaws, which are attached to the platform and base respectively.

Lower jaw. The lower jaw, Figure 4a, is mounted on the moving platform and elevated using four aluminum rods. This elevation provides two main advantages: it creates a clear line of sight to place a motion capture marker on the gnathion, and it leaves space beneath the jaw for integrating a future esophagus module. The mandibular teeth are fixed to a rigid plate and positioned slightly forward to leave room for a future tongue module. This plate already accommodates a hole for a future esophagus module.

Upper jaw. The upper jaw, Figure 4b, is mounted on a rigid frame made of aluminum rods to ensure sufficient stability and stiffness under loading. This rigidity is essential to resist the forces applied by the lower jaw during chewing. Three-axis load cells are installed on the upper jaw mounting plate to measure both vertical and lateral forces during contact. Two acrylic adaptor plates connect these load cells to the maxillary teeth. The top adaptor has a central opening reserved for a future camera, which will be used to observe food behavior during mastication.

Exchangeable teeth. Both the maxillary and mandibular teeth are designed to be easily replaceable through the use of acrylic adaptor plates. This modularity allows for testing different tooth shapes, materials, and conditions (e.g., healthy, aged, or damaged teeth), which will be important for future studies on chewing development and masticatory disorders.

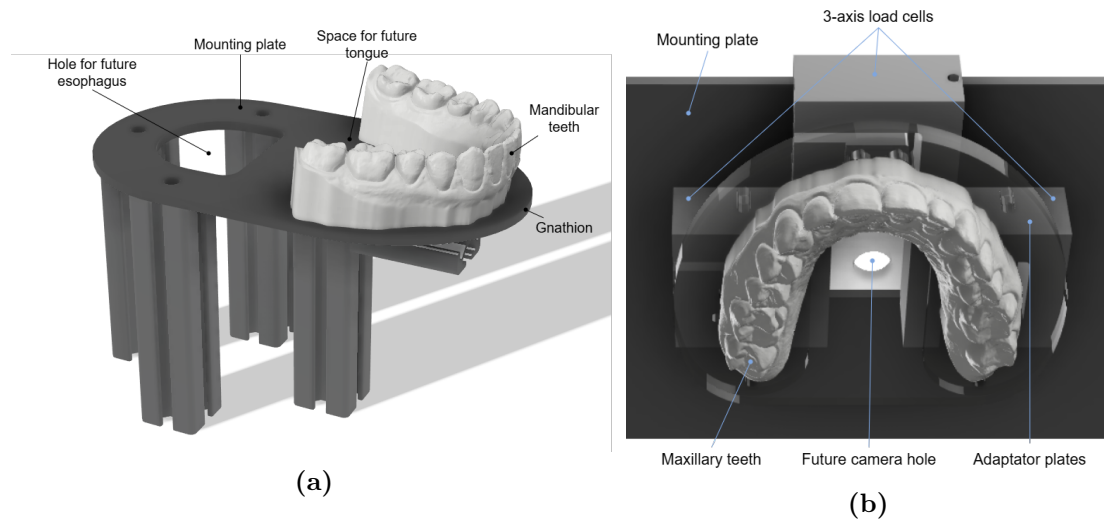


Figure 4: (a) Annotated lower jaw design. (b) Annotated upper jaw design.

2.2.4 Full assembly

Final workspace. The final design is shown in Figure 5a. Pictures of the built robot are included in Section 7.1 of the Appendix. The height of the upper jaw subsystem was set slightly below the platform's maximum vertical reach—roughly centered in the middle of its vertical workspace. This positioning ensures that the robot can apply maximum vertical force when the mandibular and maxillary teeth are in contact, while still allowing enough range to meet angular requirements during chewing. A detailed view of the vertical workspace can be found in Figure 5b. The lateral and anterior-posterior workspaces are constrained by the upper jaw frame and are approximately ± 60 mm and ± 80 mm, respectively. The base is designed as a hollow box to house the electronics described in Section 2.3.

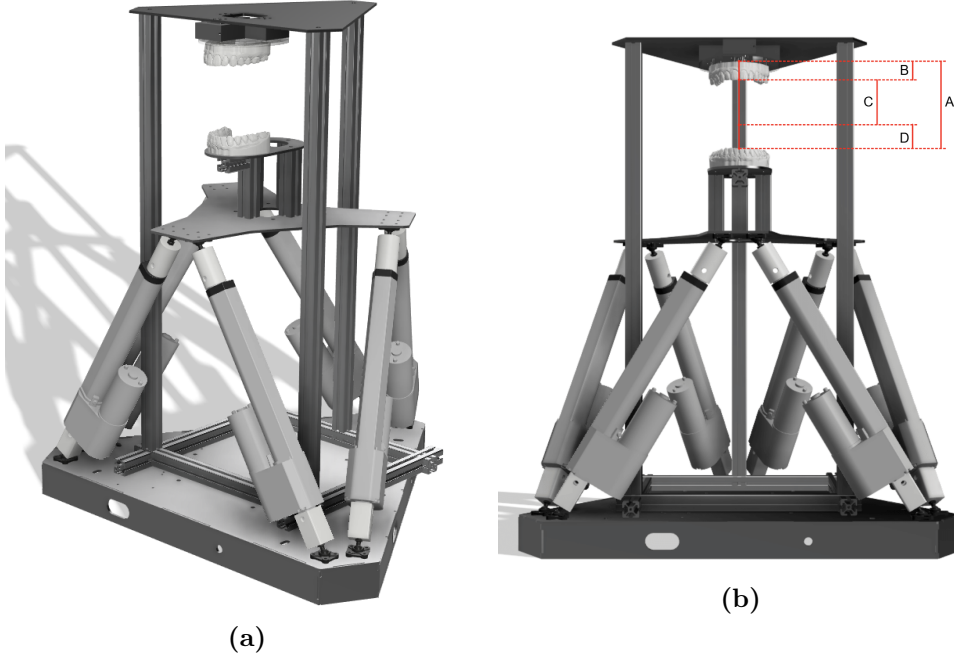


Figure 5: (a) Final design overview. (b) Workspace design: A-Full vertical workspace of 118 mm; B-Upper margin of 25 mm; C-Working chewing volume of 60 mm; D-Bottom margin of 33 mm.

Material selection. The base, platform, lower jaw mount, and upper jaw mount are all made out of steel, see Table 3. Although heavier than aluminum, steel offers significantly higher stiffness, with a Young's modulus of 190-210 GPa. This makes it a better choice for components that require high rigidity and minimal deformation under load. Additionally, steel's weldability makes it practical for future modifications—for example, adding reinforcement ribs to the upper jaw mounting plate to further improve structural stability.

Subassembly	Part	Material
Stewart Platform	Base	Steel
	Platform	Steel
	Adapter	PLA
Lower Jaw	Lower jaw mounting plate	Steel
	Mandibular teeth	PLA
Upper Jaw	Upper jaw mounting plate	Steel
	Upper jaw adapter plates	Acrylic
	Maxillary teeth	PLA

Table 3: Mechanical design materials.

Waterproofing. As the robot is designed to eventually include a saliva module, it is important to ensure that the electronics and mechanical components are protected from moisture. First, we protected the steel parts with a layer of paint to prevent rusting. Then on both the upper and bottom side of the base, a plastic sheet was added to isolate the electronics from the steel base and prevent water from entering inside the box and damaging the electronics. Finally, the linear actuators are IP54-rated, meaning they are protected against dust and splashes of water

from any direction, see Table 2.

Specifications summary. The final specifications of the chewing robot are summarized in Table 4. It is worth noting that the center of mass height is expected to decrease further once the electronic components are installed within the base enclosure.

Parameter	Value
Total mass	21 kg
Dimensions (L x W x H)	530 mm x 460 mm x 600 mm
Center of mass	150 mm above base center
Vertical force capacity ($F_{z,\max}$)	1155 N
Lateral force capacity ($F_{x,\max}$)	444 N
Anterior-posterior force capacity ($F_{y,\max}$)	385 N
Vertical workspace	118 mm
Lateral workspace	\pm 60 mm
Anterior-posterior workspace	\pm 80 mm
Working vertical chewing volume	60 mm
Actuator stroke length	101 mm
Max actuator speed (no load)	28 mm/s
Max actuator speed (full load)	21 mm/s
Moisture protection	Painted + plastic sheets + IP54-rated actuators

Table 4: Final specifications of the chewing robot.

2.3 Control system

This section describes the hardware and software architecture of the chewing robot as well as the control strategy.

2.3.1 Hardware (electronics)

A Teensy 4.1 (600 MHz ARM Cortex-M7, single-precision FPU) executes the control loop. Its key peripherals are:

- three 12 A dual DC motor drivers (DF Robot) controlling the six linear actuators;
- two multiplexers connected to :
 - six analogue inputs reading potentiometer position feedback from the linear actuators;
 - three transmitters for the load cells mounted on top of the maxilla;
- an on-board micro-SD slot used for trajectory files and calibration data.

As for the power supply, the Teensy is powered by a 5 V USB connection from the host computer, which also provides the communication link. The 3.3 V from the Teensy gives the logic levels for the motor drivers and load-cell transmitters. A 12 V AC/DC power supply powers the motor drivers directly, which in turn power the linear actuators. A 24 V AC/DC power supply is used to power the load-cell transmitters. The full electronics schematic is shown in Fig. 6. More details on the electronics connections to the Teensy 4.1 are shown in Fig. 26 in the Appendix.

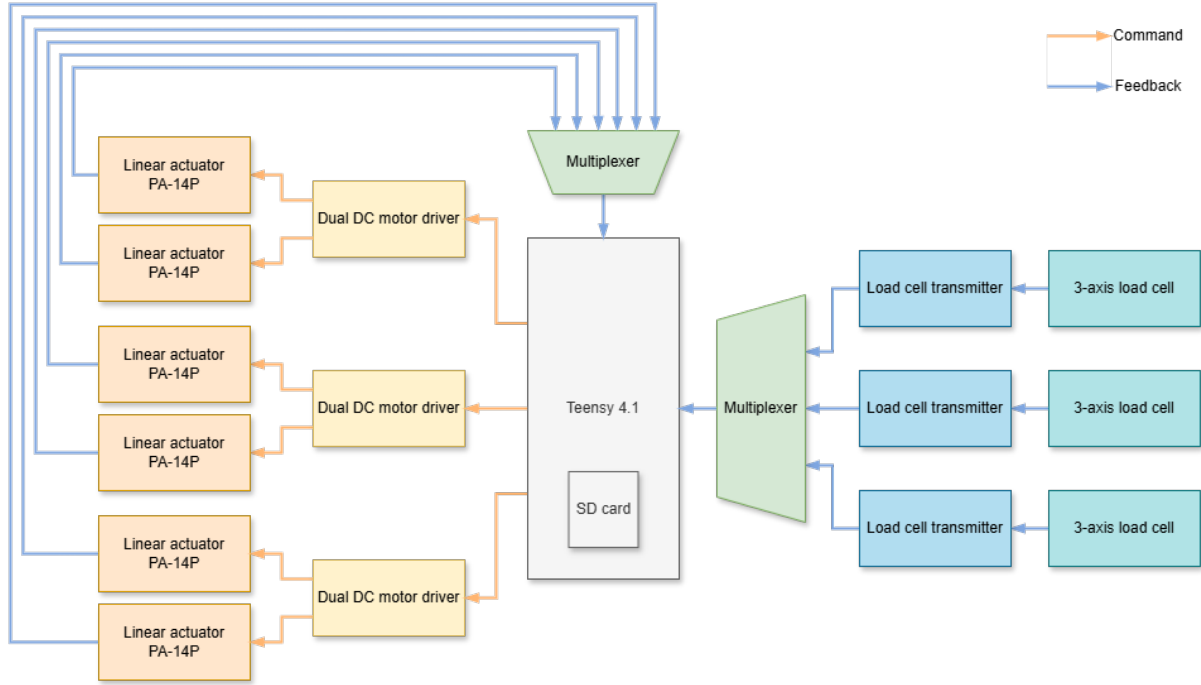


Figure 6: Electronics schematic.

2.3.2 Software architecture

The main code [12] was developed in object-oriented C++ using the Arduino framework and runs on the Teensy 4.1. The central class `RobotController` maintains the finite-state machine in Fig. 8 and manages two modules:

- `StewartPlatform`: inverse kinematics, trajectory interpolation, and low-level actuator commands;
- `ForceSensing`: continuous load-cell acquisition and filtering;

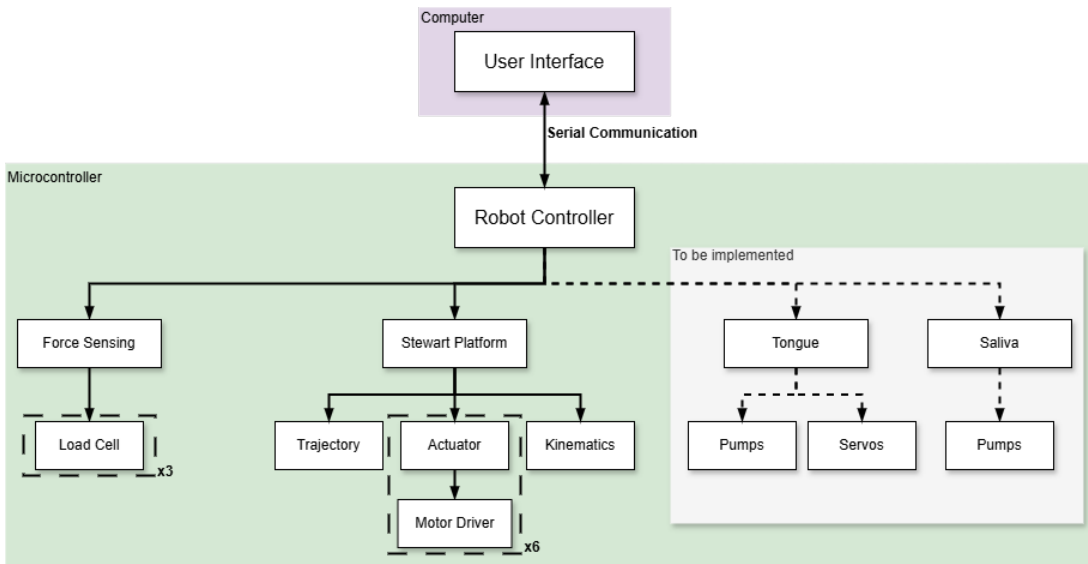


Figure 7: Overall code structure.

The controller is designed to be modular, allowing for easy addition of new modules such as a tongue or saliva module in the future.

The three controller states are:

1. **Stop** – return to home pose; reload trajectory if the user selects a new file;
2. **Calibrate** – user can manually change the initial (x, y, z) position via the GUI;
3. **Move** – replay the selected trajectory.



Figure 8: Robot controller state machine.

The host PC runs a lightweight python GUI built with PyQt5, which is used to send high-level commands, such as initiating state transitions. It also collects sensory feedback through the serial terminal. Upon pressing the Stop button, the interface generates plots from the recorded data. The GUI layout is shown in Figure 9.

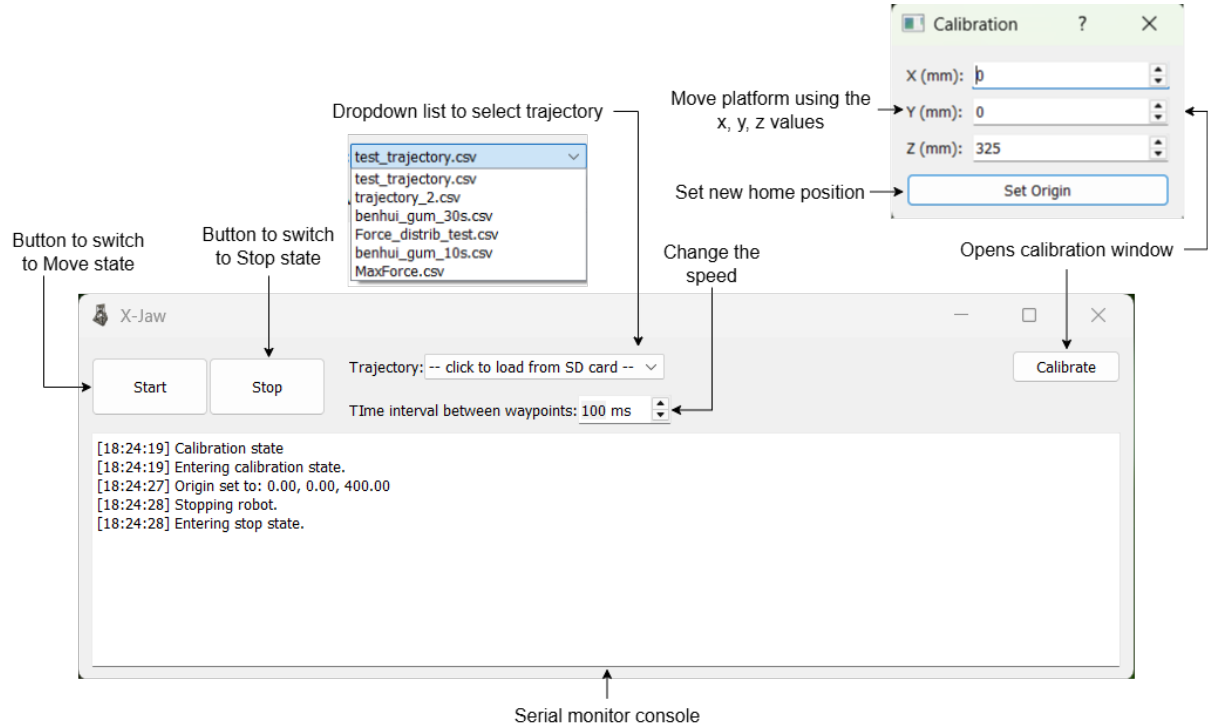


Figure 9: Robot controller GUI.

2.3.3 Stewart platform control

The Stewart platform is controlled by the `StewartPlatform` class, which manages the trajectory, platform kinematics, and high-level actuator control. Its real-time loop executes every 10 ms (100 Hz). The platform follows a 3D trajectory (x, y, z , roll, pitch, yaw) from a .csv file on the micro-SD card. See section 2.4 for details on the recording protocol and data processing. Each

pose is defined by its position $\mathbf{t} = (x, y, z)$ and orientation given by the Euler angles (ϕ, θ, ψ) , which are the roll, pitch, and yaw angles respectively. The trajectory is then interpolated using a Catmull-Rom spline with a fixed time step chosen by the user.

Inverse kinematics For each pose in the trajectory, **Kinematics** computes the lengths of the six linear actuators that will achieve the desired pose of the platform, i.e. the inverse kinematics. First, let's define our system. The base is defined as the global reference frame with orthogonal axes (x , y , z), while the platform is associated with a local orthogonal coordinate system (x' , y' , z'). Figure 10 shows a visualization of these axes. The platform has six degrees of freedom relative to the base: three translational and three rotational. To account for the platform's rotation, we use the standard rotation matrix $R(\phi, \theta, \psi)$, which is defined as the product of three rotation matrices about the Z , Y , and X axes:

$$R(\phi, \theta, \psi) = R_Z(\psi)R_Y(\theta)R_X(\phi) = \begin{pmatrix} \cos \psi & -\sin \psi & 0 \\ \sin \psi & \cos \psi & 0 \\ 0 & 0 & 1 \end{pmatrix} \begin{pmatrix} \cos \theta & 0 & \sin \theta \\ 0 & 1 & 0 \\ -\sin \theta & 0 & \cos \theta \end{pmatrix} \begin{pmatrix} 1 & 0 & 0 \\ 0 & \cos \phi & -\sin \phi \\ 0 & \sin \phi & \cos \phi \end{pmatrix}$$

In our case, the center of rotation is the gnathion, defined as a fixed point \mathbf{c} and visualized in Figure 4a, rather than the origin of the platform. Therefore, the platform joints \mathbf{p}_i , i being the actuator index, are first rotated about the gnathion and then translated by the user-defined home position $\mathbf{T} = (x, y, z)$, resulting in the global coordinates of the platform joints:

$$\mathbf{q}_i = R(\mathbf{p}_i - \mathbf{c}) + \mathbf{c} + \mathbf{T}.$$

Figure 11 shows the kinematic schematic for the i^{th} actuator. Finally, the actuator length is the Euclidean distance to the fixed base joint \mathbf{b}_i :

$$\ell_i = \|\mathbf{q}_i - \mathbf{b}_i\|_2.$$

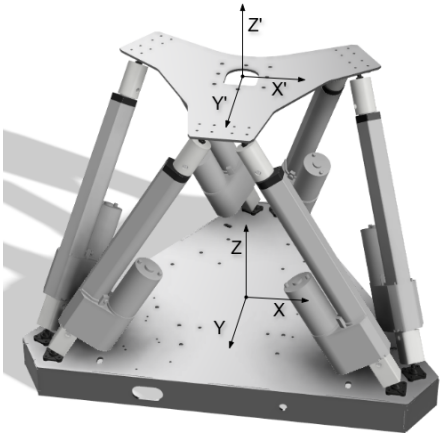


Figure 10: Robot referential.

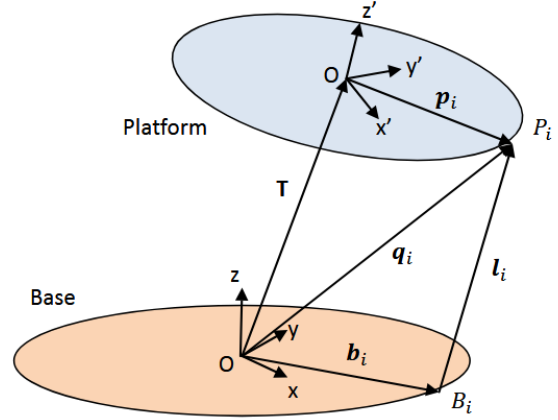


Figure 11: Schematic of the Stewart platform kinematics for the i^{th} actuator [13].

PI controller For each actuator, its desired length is sent to a PI position controller, see Figure 12. The PI gain values are set to $K_P = 25$ and $K_I = 0.1$, which were determined empirically to achieve a good trade-off between responsiveness and stability. An anti-windup mechanism is implemented to prevent the integral term from growing too large, which could

lead to overshooting. To minimize the noise of the potentiometer feedback, we apply a low-pass filter averaging the last 10 samples.

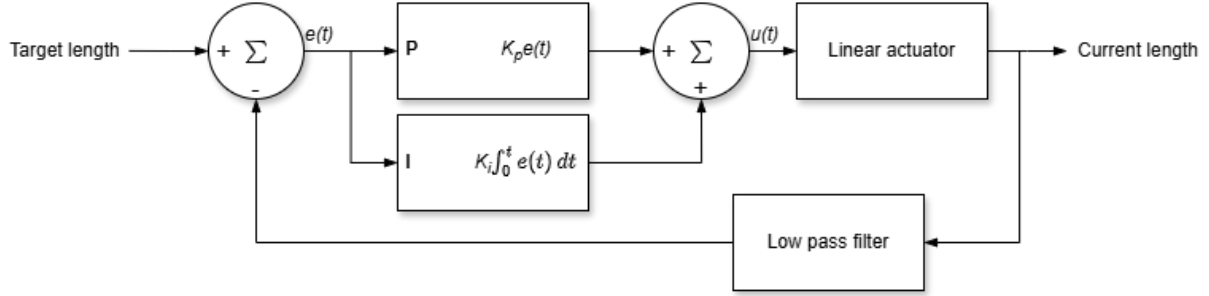


Figure 12: Position PI controller for the linear actuators.

2.3.4 Force sensing

The **ForceSensing** module is responsible for acquiring and processing data from the three triaxial load cells mounted on the upper jaw. Each load cell is represented by an instance of the **LoadCell** class, which performs signal conditioning on the raw sensor data. Specifically, a low-pass filter is applied by averaging the last 10 samples to reduce high-frequency noise.

According to the manufacturer’s calibration data, the load cell output from the transmitter is sufficiently linear for direct mapping, see Figure 13. Based on this, the **LoadCell** class linearly scales the filtered signal to a calibrated force range of [0, 500] N. To eliminate static bias introduced by preloading or assembly stress, each load cell is automatically tared at system startup.

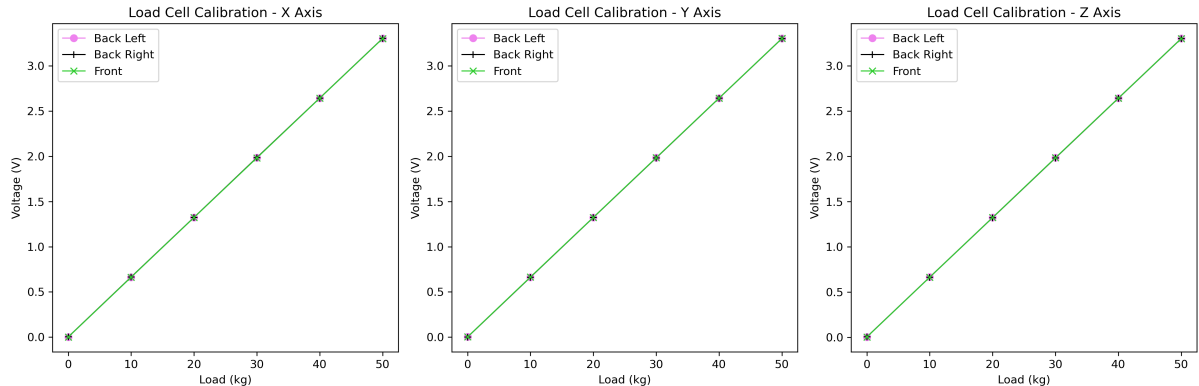


Figure 13: Load cell calibration data.

The **ForceSensing** module aggregates the force data from all three load cells to compute the total force applied on the upper jaw. Since each load cell only measures force in the positive direction of its axis, their physical orientation must be accounted for during summation. This configuration is illustrated in Figure 14. The total forces in the x, y, and z directions are calculated as:

$$F_{x,total} = F_{x,front} + F_{x,backL} - F_{x,backR}, \quad (5)$$

$$F_{y,total} = F_{y,front} + F_{y,backL} - F_{y,backR}, \quad (6)$$

$$F_{z,total} = F_{z,front} + F_{z,backL} + F_{z,backR}. \quad (7)$$

For now, the **ForceSensing** module primarily serves as a safety mechanism and force feedback recording. If the total measured force exceeds predefined thresholds—200 N in the z-direction, 60 N in x, or 50 N in y—the module fails and triggers **RobotController** to transition to **Stop** mode to prevent damage to the robot.

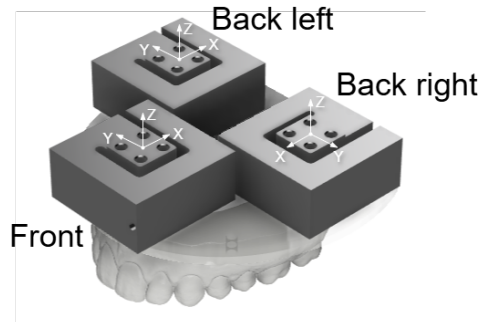


Figure 14: Load cells orientation.

2.4 Data acquisition and processing

2.4.1 Subjects

Two healthy adult volunteers (author and project supervisor) participated in this pilot recording. Informed consent was obtained from both participants. Owing to time constraints and the exploratory nature of the study, no additional subjects were recruited.

2.4.2 Motion-capture acquisition



Figure 15:
Marker
placement.

Mandibular motion was recorded with a five-camera OptiTrack system sampling at 120 Hz. Four reflective markers arranged in a square were attached to the forehead and served as a head-fixed reference frame. A second set of three markers forming a triangle was placed on the gnathion. Figure 15 shows the marker placement. Two additional lip markers were recorded but later discarded because a single marker cannot encode orientation [14, 15]. The subject then performed the motion sequences listed in Table 5. Each frame was saved by Motive as a .csv file that contains the 3-D marker positions (in millimetres) and the orientation of each marker set as quaternions. The calibrated volume had a residual error of 0.3 mm.

Food	Motion	Optional: Duration
Empty mouth	20× open–close cycles	—
Chewing gum (Xylit-Pro, <i>Excitemint</i>)	Random side chewing	2 min
	Right-side chewing	1 min
	Left-side chewing	1 min
	Front-teeth-only chewing	1 min
Biscuits (Bretzeli, <i>Kambli</i>)	random chewing	—
	front-teeth chew → right-side chew	—
	front-teeth chew → left-side chew	—
	<i>fast</i> random chewing	—
	<i>slow</i> random chewing	—

Table 5: Recording protocol. *Notes:* For chewing-gum trials the first run began with an unchewed piece and the same gum was kept for all subsequent motions. For biscuit trials each run started with an empty, closed mouth; the subject then placed a biscuit, chewed as instructed, and swallowed.

2.4.3 Data processing

To reduce high-frequency noise in the motion capture data, a 4th-order Butterworth low-pass filter was applied, with a cutoff frequency set at 6 Hz. This value was chosen based on reported human mastication frequencies, typically ranging from 1-3 Hz and up to 6 Hz when the subjects are instructed to chew at higher rates [16].

Following filtering, the gnathion marker motion was transformed to the head-fixed marker reference frame using rotation matrices, effectively compensating for head motion during recording. The next step was to convert the data into the robot's coordinate system, defined as follows:

- the X axis is horizontal, pointing to the subject's left;
- the Y axis is horizontal, pointing forward;
- the Z axis is vertical, pointing upwards.

Due to uncertainty about the absolute orientation of the OptiTrack coordinate system, we performed Principal Component Analysis (PCA) on the recorded open-close cycles to estimate the appropriate rotation matrix. The underlying assumption is that the largest motion range (i.e., the first principal component) corresponds to the robot's Z-axis, the second to the Y-axis, and the third to the X-axis, following the hierarchy of motion amplitude typical in mastication dynamics during mouth opening [17]. As the principal components (PC) are orthogonal, the resulting matrix forms a valid orthonormal basis. The rotation matrix is then constructed by assigning the principal components as its column vectors.

Upon visual inspection of the data, we flipped the X and Z axes so that both decrease during jaw opening, ensuring alignment with the robot's coordinate conventions and human data [18]. All positional and rotational data were then projected into this new reference frame using the resulting rotation matrix:

$$R = \begin{pmatrix} -\text{PC}_1 & \text{PC}_2 & -\text{PC}_3 \end{pmatrix}.$$

To express orientation, the recorded quaternions were converted to Euler angles, providing the roll, pitch, and yaw components used by the robot's Stewart platform.

Then, to align the trajectory with the robot's origin, positional and rotational offsets were computed from the final stationary segment of the recording. The last second of the dataset—during which the subject remained still—was used to compute the median values of position and orientation. These offsets were subtracted from the full dataset to ensure proper alignment with the robot's neutral pose.

Finally, the most suitable trajectory segments were selected for replay on the robot. Selection was based on the smoothness of motion and the absence of outliers or artifacts in the recorded data.

3 Results

3.1 Motion captured chewing trajectories

Figure 16 shows a trajectory obtained using the method described in Section 2.4. The vertical displacement clearly reveals cyclic jaw movements, identifiable by recurring peaks that correspond to the opening and closing phases of the chewing cycle. The horizontal components (x and y) show a pattern consistent with reported human data [18].

The orientation data on the other hand is less reliable as no clear pattern can be seen throughout the trajectory. Several factors described in Section 4.2.3 may contribute to this inaccuracy.

Nonetheless, the trajectory remains sufficiently accurate to evaluate the robot’s position control performance and serves as a useful initial benchmark.

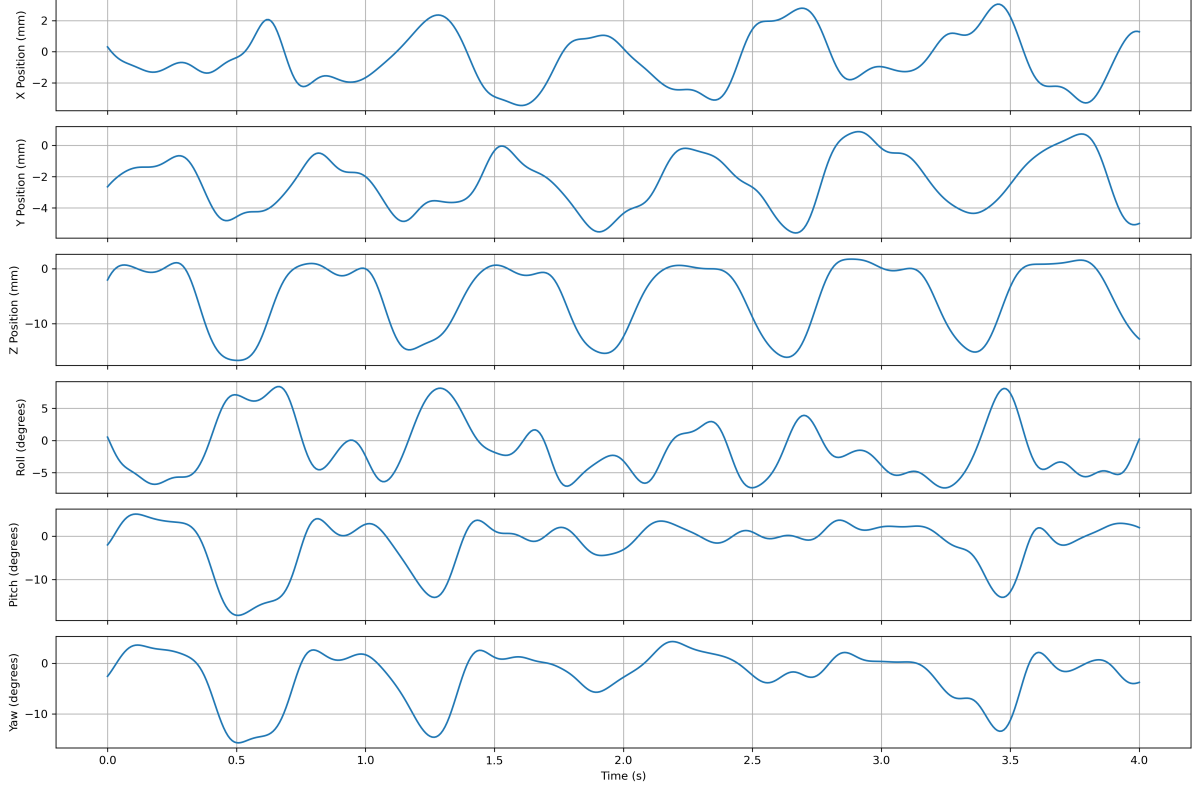


Figure 16: Random side chewing gum mastication trajectory.

3.2 Position control

To evaluate the performance of the position control system, we investigated the robot’s ability to track a predefined trajectory at varying speeds. In this context, “speed” refers to the time interval between consecutive trajectory points. While the motion capture data was recorded at 120 Hz (approximately every 8.3 ms), the playback was tested at longer intervals: 40 ms (25 Hz), 50 ms (20 Hz), 60 ms (16.67 Hz), 70 ms (14.29 Hz), 80 ms (12.5 Hz), 90 ms (11.11 Hz), and 100 ms (10 Hz).

For this test, a 10-second segment of chewing motion was used. Figure 18 illustrates the tracking performance of actuator 2 at the various speeds. To quantify timing discrepancies, we conducted a cross-correlation analysis between the target and actual actuator lengths, providing both time delays (Figure 18) and cross-correlation coefficients (Figure 19).

The results show that at a sampling interval of 100 ms (10 Hz), the robot tracks the trajectory well, with an average delay of 0.7 s and cross-correlation coefficients exceeding 0.975. However, performance degrades significantly at higher speeds (i.e., shorter intervals), as reflected in both increased delays and a drop in correlation values—especially below 80 ms, where the tracking error becomes pronounced and key trajectory peaks are missed.

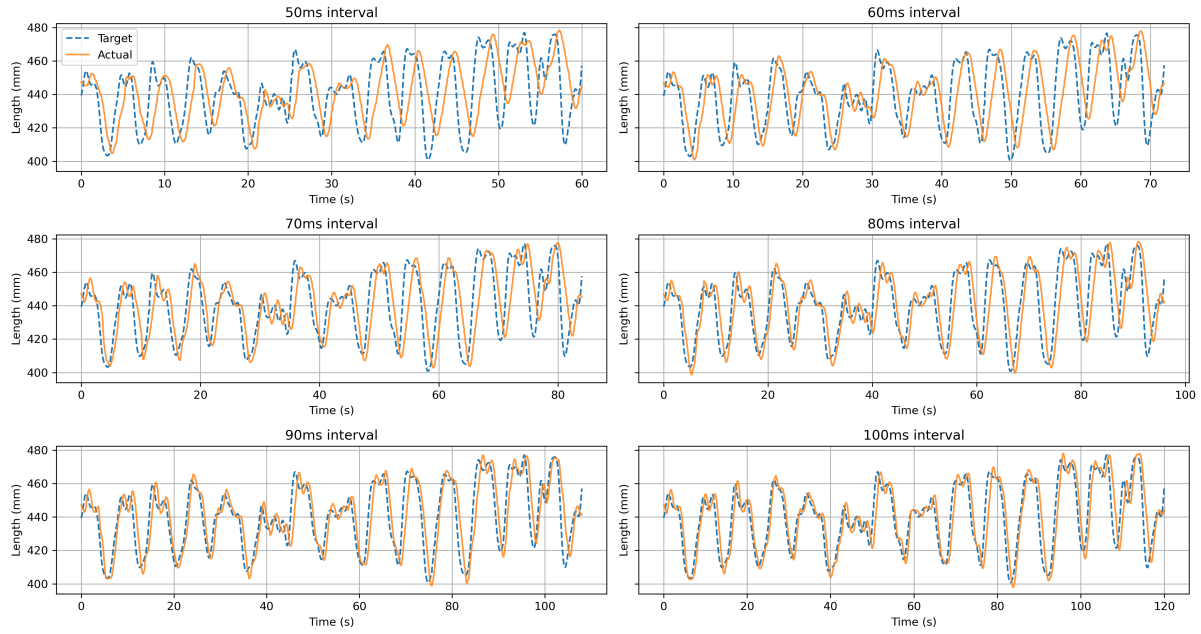


Figure 17: Performance of position control of actuator 2 across different time intervals between trajectory points.

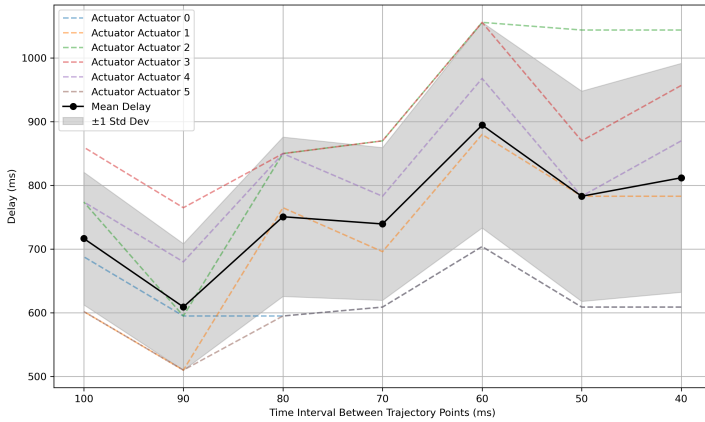


Figure 18: Delays between target and actual actuator length across different time intervals.

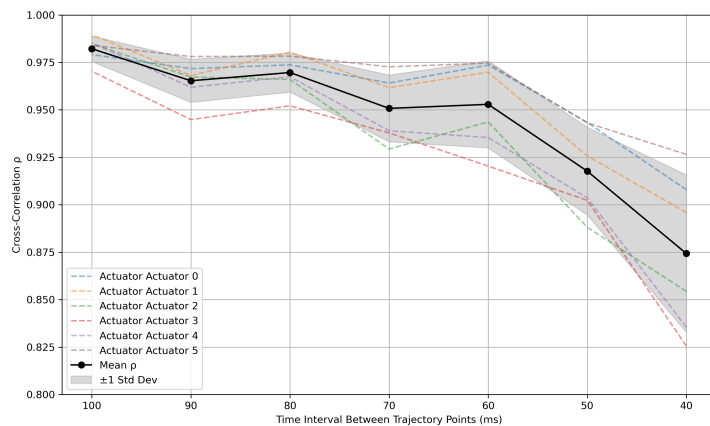


Figure 19: Cross-correlation coefficients across actuators for different time intervals.

3.3 Force analysis

3.3.1 Maximum force

The robot's vertical force generation capabilities were assessed using manual control mode normally used to set the robot's home position during calibration. The platform was driven at its highest height under active force feedback while avoiding structural failure. The upper bound of the robot's vertical force output was constrained by the stiffness of the upper jaw structure, which visibly bent under high vertical force. Table 6 shows the maximum forces recorded by the three load cells during this test, see Figure 14. for the load cell positions. The results shows that most of the vertical force is applied to the back load cells, which reflects the anatomical load pattern during full occlusion, where the molars bear the majority of chewing forces. Similarly for the antero-posterior force (F_y) where most of it is applied on the front load cell, i.e. the incisors. The total vertical, lateral and antero-posterior force output of the robot are well within the average forces during healthy human chewing [9], although F_z is below the maximum bite force from Table 1.

Load Cell	$F_{z,max}$ (N)	$F_{y,max}$ (N)	$F_{x,max}$ (N)
Back Right Load Cell	124.63	59.64	123.85
Back Left Load Cell	124.63	23.95	67.84
Front Load Cell	66.28	81.38	123.07
Total Force	315.98	103.08	125.71

Table 6: Maximal forces recorded by the load cells during the force test.

3.3.2 Force feedback distribution

To evaluate the spatial resolution of the force sensing system, we applied a simple vertical trajectory while placing a piece of gum-like material at three distinct positions between the teeth: back right, front, and back left. The vertical force output from each of the three load cells was recorded and shown in Figure 20.

The plot clearly shows three distinct peaks corresponding to the three test positions, confirming the system's capability to localize force application across the dental arch. Additionally, when force is applied at the back, the front load cell registers a smaller secondary response. This is consistent with the mechanical coupling in the mounting structure, as the front load cell is physically situated between the two rear ones.

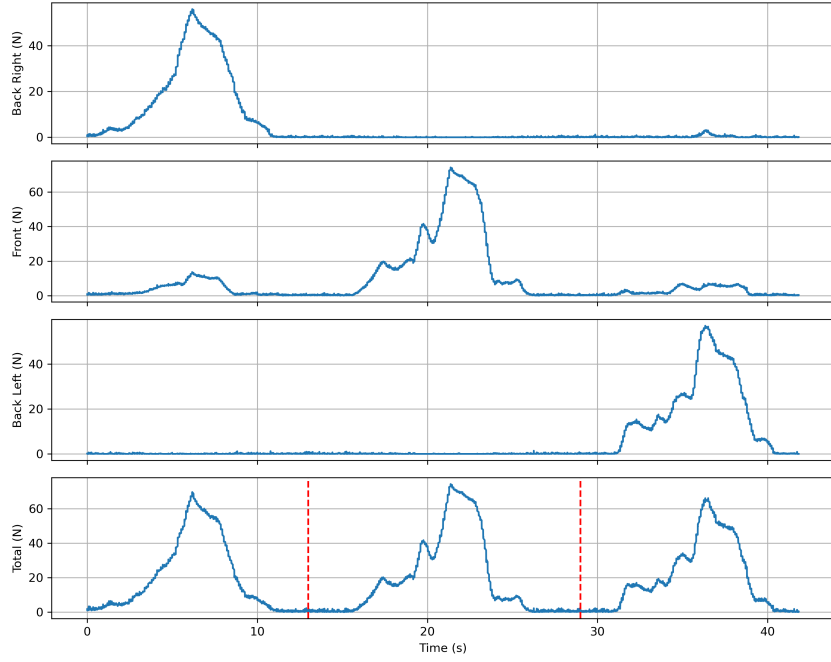


Figure 20: Vertical force output across three load cells during chewing with localized gum placement. The red lines separate the three gum positions: back right, front, and back left.

3.4 Scalability and modularity

A central goal of the project was to build a scalable platform for future modules such as a tongue, saliva pumps, and an esophagus. As described in Section 2.2, the mechanical design already accommodates these additions, including space for internal cameras to observe the chewing process. A rendering of the proposed tongue module is shown in Figure 21. These design decisions were made in collaboration with project supervisor Benhui Dai.

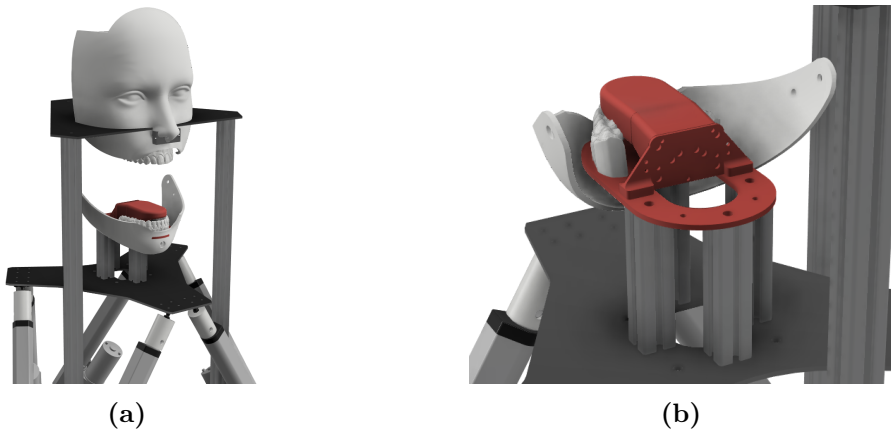


Figure 21: Future tongue module rendering. (a) Front view, (b) Back view.

The control system, detailed in Section 2.3, was developed with similar modularity in mind. Its finite-state machine architecture supports the easy integration of new components such as actuators and sensors for additional subsystems.

The robot's modularity also extends to the dental elements. Maxillary and mandibular teeth are mounted on replaceable acrylic adaptors, allowing for rapid testing of different dentitions.

Combined with flexible trajectory loading, this makes the system suitable for a wide range of experimental and clinical scenarios.

4 Discussion

4.1 Summary of Findings

The chewing robot satisfies every functional requirement listed in Table 1—save for peak bite force—while still matching the average occlusal forces. Motion-capture trajectories are successfully replicated at one-twelfth of the human chewing rates, demonstrating that the 6-DoF platform can mimic human chewing kinematics. Integrated tri-axial load-cell arrays provide spatially resolved force data, enabling 3-D feedback for future closed-loop force control and basic safety mechanism. A layered architecture—mechanics, modular robot controller, and a user-friendly GUI—keeps the system open for upgrades such as an actuated tongue, saliva circuit, or esophagus module. In short, the current design delivers human-scale motion and average chewing forces today, while leaving clear hooks for future biomimetic extensions.

4.2 Limitations

Although this work represents an important first step towards a complete chewing robot, several limitations remain that currently prevent the system from accurately mimicking real mastication.

4.2.1 Mechanical design

The robot currently lacks a closed mouth, which would cause food to fall out during chewing. For a functional mastication process, particularly with soft or fragmented food items, a sealed oral cavity is essential to retain and guide the bolus.

The current teeth are 3D printed in PLA, a material that is not hard enough to reproduce the mechanical properties of real enamel. Furthermore, the surface finish of 3D printed PLA is inherently rough, which introduces friction and causes jitter when the teeth slide against each other. This affects both motion fidelity and safety of the robot.

Structural bending of the upper jaw during high-force tests limits vertical force output to 300 N—well below the theoretical 1155 N—introducing instability and limiting our ability to reproduce realistic occlusal forces.

The current Stewart platform is non-compliant and replays motion with limited precision—an unfavorable combination for full occlusion, where natural teeth can slide and interact with high dexterity while the robot risks damage during such contact.

4.2.2 Electronics and control

The current control loop lacks force feedback and bio-inspiration. It also introduces a 0.7 s delay at 10 Hz, which is too high for real-time interaction with future modules like the tongue or saliva systems.

Position feedback from the built-in potentiometers is too coarse for precise motion tracking. Higher-resolution sensors, such as optical encoders, would improve accuracy. Additionally, re-

lying on actuators with integrated feedback limits selection; using external sensors could allow for faster, more compact motors.

4.2.3 Motion capture recordings

The accuracy of the recorded jaw motion is limited by the motion capture system, with a calibration error of around 0.3 mm—significant given that chewing displacements occur on a millimeter scale. Additionally, tracking was done using a marker on the gnathion, a skin-based reference point, which introduces error due to skin movement relative to the jawbone. As a result, the recorded trajectories lack full biomechanical accuracy. Alternative methods like kinesiography [19], which track a magnet fixed to the jaw, offer higher spatial and temporal precision and would be better suited for generating reliable chewing datasets.

4.3 Future Work

This section outlines key directions for improving both the mechanical design and control of the chewing robot to move closer to a functional and autonomous chewing system.

4.3.1 Mechanical design improvements

Future designs should feature a closed oral cavity using a flexible membrane—such as latex or polyurethane—and a transparent membrane would allow visual monitoring of the food during mastication.

The current PLA teeth should be replaced with more rigid materials, such as 3D-printed resin or anatomical dental models, to better replicate the mechanical properties of real teeth.

The upper jaw assembly should be reinforced to allow for higher vertical force. This could be achieved by welding structural ribs onto the mounting plate or attaching an external aluminum rod for additional support.

Additionally, a compliant layer between the lower jaw and the platform could be added to allow for more realistic interaction between maxillary and mandibular teeth during occlusion.

Finally, the tongue, saliva, and esophagus modules should be developed to enhance the robot's functionality and mimic the full chewing process. Two cameras, RGB and thermal, should be mounted inside the mouth to monitor it.

4.3.2 Control system improvements

The current closed-loop position-based strategy should be changed to managing both position and force in a dynamic, compliant manner, such as impedance control [20].

Future iterations of the software could leverage the recorded human chewing motion data to identify a small set of representative motion patterns using PCA. Mixing these trajectories would allow the robot to switch between different chewing motions based on sensory input or task requirements. This would enable autonomous mastication and food processing, paving the way for biologically accurate studies of chewing mechanics.

To implement the above approach, the suitability of the current motion dataset must be assessed. If inadequate, new recordings—ideally using more accurate motion capture methods—will be

necessary.

5 Conclusion

This project presented the design and development of a novel chewing robot capable of reproducing jaw motions using a Stewart platform. The mechanical design, control system, and data processing pipeline were developed with scalability and modularity in mind, laying the groundwork for a more complete biomimetic mastication system.

The robot successfully replicates simplified human jaw trajectories using motion capture data and demonstrates the ability to generate average chewing forces. The inclusion of force sensing enables 3D distributed force feedback and basic safety mechanisms. The modular control system and mechanical design allow for future integration of additional features, such as a tongue, saliva module, or esophagus.

Despite these achievements, the robot in its current form is not yet capable of full chewing functionality. Limitations in mechanical compliance, control accuracy, sensing precision, and teeth design prevent accurate and robust reproduction of natural mastication. Additionally, the current motion capture methodology introduces errors that limit the fidelity of recorded trajectories.

Nonetheless, the system serves as a strong foundation for future work. Improvements in control strategy, sensing, compliance, and anatomical fidelity—combined with more accurate motion datasets—will enable the robot to more closely replicate the biomechanics of human chewing.

6 References

- [1] Ahmad Mahmood Tahir et al. “Architecture and design of a robotic mastication simulator for interactive load testing of dental implants and the mandible”. In: *The Journal of Prosthetic Dentistry* 122.4 (2019), 389.e1–389.e8. ISSN: 0022-3913. DOI: [10.1016/j.prosdent.2019.06.023](https://doi.org/10.1016/j.prosdent.2019.06.023). URL: <https://www.sciencedirect.com/science/article/pii/S0022391319304810>.
- [2] Sandip Panda et al. “A novel electro-mechanical chewing system for food oral processing research: A comprehensive design approach”. In: *Innovative Food Science and Emerging Technologies* 95 (2024), p. 103735. ISSN: 1466-8564. DOI: [10.1016/j.ifset.2024.103735](https://doi.org/10.1016/j.ifset.2024.103735). URL: <https://www.sciencedirect.com/science/article/pii/S1466856424001747>.
- [3] Kazem Alemzadeh et al. “Development of a Chewing Robot with Built-in Humanoid Jaws to Simulate Mastication to Quantify Robotic Agents Release from Chewing Gums Compared to Human Participants”. English. In: *IEEE Transactions on Biomedical Engineering* 68.2 (Feb. 2021), pp. 492–504. ISSN: 0018-9294. DOI: [10.1109/TBME.2020.3005863](https://doi.org/10.1109/TBME.2020.3005863).
- [4] K Alemzadeh and D Raabe. “Prototyping artificial jaws for the Bristol Dento-Munch Robo-Simulator; ‘A parallel robot to test dental components and materials’. English. In: (2007). ISBN: 9781424407873 Name and Venue of Conference: 29th Annual International Conference of the IEEE Engineering in Medicine and Biology Society - Lyon, France Conference Organiser: IEEE, EMBS, SFGBM, pp. 1453–1456. DOI: [10.1109/IEMBS.2007.4352574](https://doi.org/10.1109/IEMBS.2007.4352574).
- [5] Seung-Ju Lee et al. “Design of mastication robot with life-sized linear actuator of human muscle and load cells for measuring force distribution on teeth”. In: *Mechatronics* 51 (2018), pp. 127–136. ISSN: 0957-4158. DOI: <https://doi.org/10.1016/j.mechatronics.2017.11.013>. URL: <https://www.sciencedirect.com/science/article/pii/S0957415817301769>.
- [6] Johannes H. Koolstra. “Dynamics of the Human Masticatory System”. In: *Critical Reviews in Oral Biology & Medicine* 13.4 (2002), pp. 366–376. ISSN: 1045-4411. DOI: [10.1177/154411130201300406](https://doi.org/10.1177/154411130201300406). URL: <https://doi.org/10.1177/154411130201300406>.
- [7] K.C. Julien et al. “Normal masticatory performance in young adults and children”. In: *Archives of Oral Biology* 41.1 (1996), pp. 69–75. ISSN: 0003-9969. DOI: [https://doi.org/10.1016/0003-9969\(95\)00098-4](https://doi.org/10.1016/0003-9969(95)00098-4). URL: <https://www.sciencedirect.com/science/article/pii/0003996995000984>.
- [8] Charles H. Gibbs et al. “Maximum clenching force of patients with moderate loss of posterior tooth support: A pilot study”. In: *The Journal of Prosthetic Dentistry* 88.5 (2002), pp. 498–502. ISSN: 0022-3913. DOI: <https://doi.org/10.1067/mpr.2002.129062>. URL: <https://www.sciencedirect.com/science/article/pii/S0022391302002585>.
- [9] Sarah C. Woodford et al. “Muscle and joint mechanics during maximum force biting following total temporomandibular joint replacement surgery”. In: *Biomechanics and Modeling in Mechanobiology* 23.3 (2024), pp. 809–823. ISSN: 1617-7959. DOI: [10.1007/s10237-023-01807-1](https://doi.org/10.1007/s10237-023-01807-1). URL: <https://doi.org/10.1007/s10237-023-01807-1>.
- [10] Vassil Svechtarov et al. “Mandibular range of motion and its relation to temporomandibular disorders”. In: *Scripta Scientifica Medicinae Dentalis* 1.1 (2015).
- [11] Oren Masory and Jian Wang and. “Workspace evaluation of Stewart platforms”. In: *Advanced Robotics* 9.4 (1994), pp. 443–461. DOI: [10.1163/156855395X00508](https://doi.org/10.1163/156855395X00508). eprint: <https://doi.org/10.1163/156855395X00508>. URL: <https://doi.org/10.1163/156855395X00508>.
- [12] Barbara De Groot. *RoboticsJawArduino*. 2025. URL: <https://github.com/Bdg9/RoboticsJawArduino> (visited on 06/20/2025).

-
- [13] Unknown. *DIY Stewart Platform*. 2024. URL: <https://cdn.instructables.com/ORIG/FFI/8ZXW/I55MMY14/FFI8ZXWI55MMY14.pdf> (visited on 06/15/2025).
 - [14] Steven Mills et al. “Principal Component Representations of Chewing Motion”. In: IVCNZ '14 (2014), pp. 218–223. DOI: [10.1145/2683405.2683434](https://doi.org/10.1145/2683405.2683434). URL: <https://doi.org/10.1145/2683405.2683434>.
 - [15] Meg Simione et al. “Differing structural properties of foods affect the development of mandibular control and muscle coordination in infants and young children”. In: *Physiology & Behavior* 186 (2018), pp. 62–72. ISSN: 0031-9384. DOI: <https://doi.org/10.1016/j.physbeh.2018.01.009>. URL: <https://www.sciencedirect.com/science/article/pii/S0031938418300155>.
 - [16] T. Morimoto et al. “Frequency-dependent Modulation of Rhythmic Human Jaw Movements”. In: *Journal of Dental Research* 63.11 (1984). PMID: 6594375, pp. 1310–1314. DOI: [10.1177/00220345840630111201](https://doi.org/10.1177/00220345840630111201).
 - [17] K.H. Travers et al. “Associations between incisor and mandibular condylar movements during maximum mouth opening in humans”. In: *Archives of Oral Biology* 45.4 (2000), pp. 267–275. ISSN: 0003-9969. DOI: [https://doi.org/10.1016/S0003-9969\(99\)00140-5](https://doi.org/10.1016/S0003-9969(99)00140-5). URL: <https://www.sciencedirect.com/science/article/pii/S0003996999001405>.
 - [18] Prafulla Thumati, Roshan Thumati, and John Radke. “Changes in Objective Masticatory Measurements after Prosthodontic Treatments”. In: *Advanced Dental Technologies and Techniques* 2.1 (2020). Published online 12 Jan 2020, pp. 69–82. URL: <https://adtt.scholasticahq.com/article/11728-changes-in-objective-masticatory-measurements-after-prosthodontic-treatments>.
 - [19] S Gomes et al. “Masticatory features, EMG activity and muscle effort of subjects with different facial patterns”. In: *Journal of oral rehabilitation* 37 (Nov. 2010), pp. 813–9. DOI: [10.1111/j.1365-2842.2010.02075.x](https://doi.org/10.1111/j.1365-2842.2010.02075.x).
 - [20] L. Huang et al. “Design of a position and force control scheme for 6RSS parallel robots and its application in chewing robots.” In: *International Journal of Humanoid Robotics* 07.03 (2010), pp. 477–489. DOI: [10.1142/S0219843610002210](https://doi.org/10.1142/S0219843610002210). URL: <https://doi.org/10.1142/S0219843610002210>.

7 Appendix

7.1 Real robot pictures

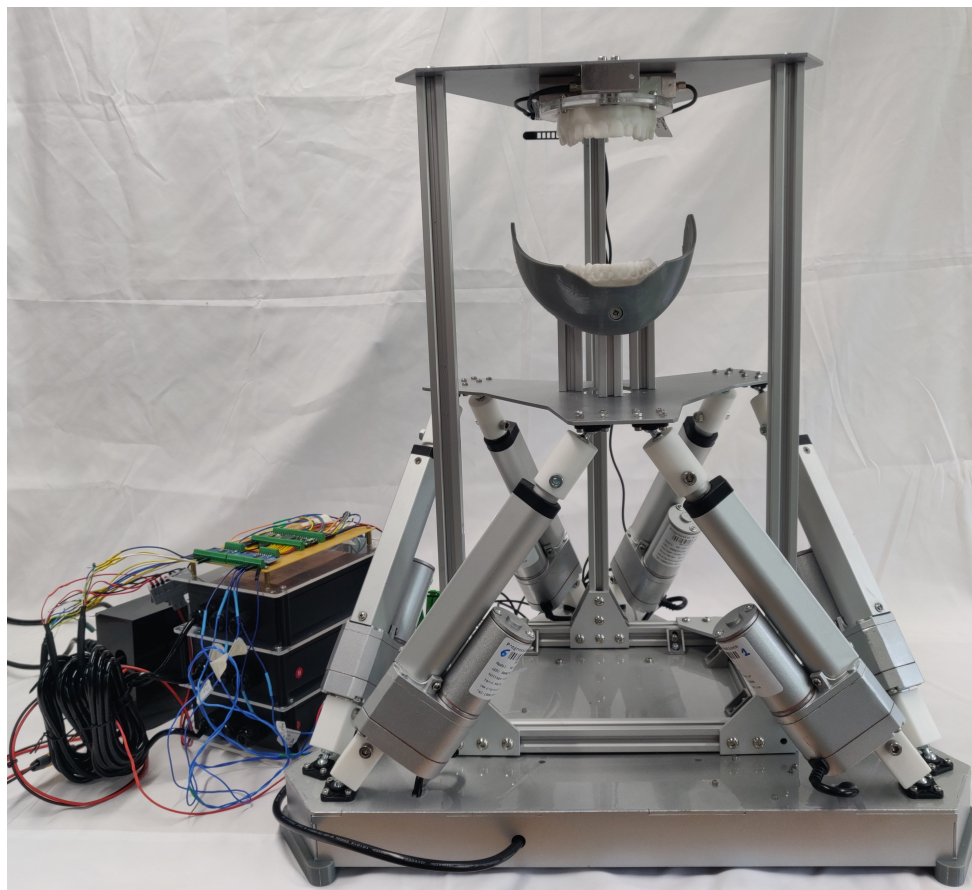


Figure 22: Picture of the robot overview, including electronics on the left side.

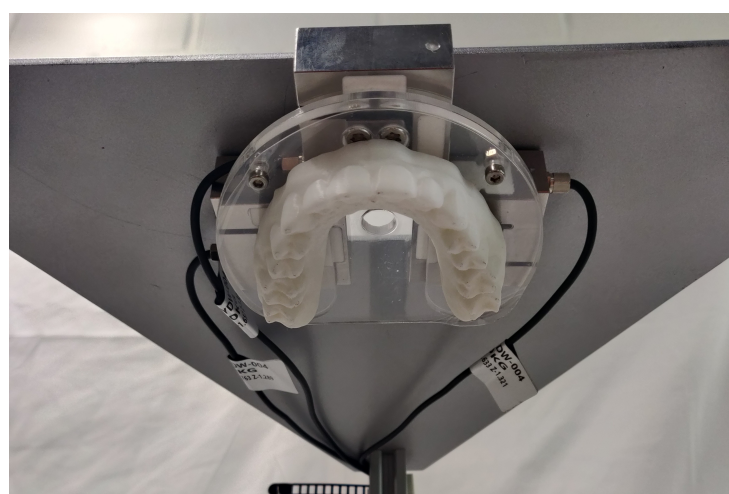


Figure 23: Picture of the upper jaw close-up.



Figure 24: Picture of the lower jaw close-up.

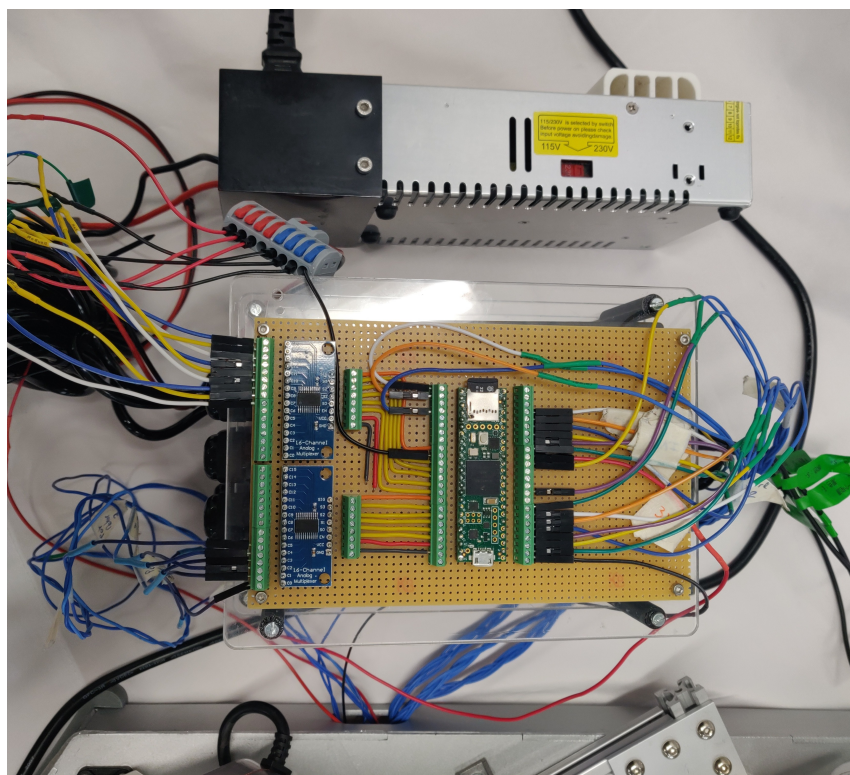


Figure 25: Picture of the main electronics close-up.

7.2 Electronics connections to Teensy 4.1

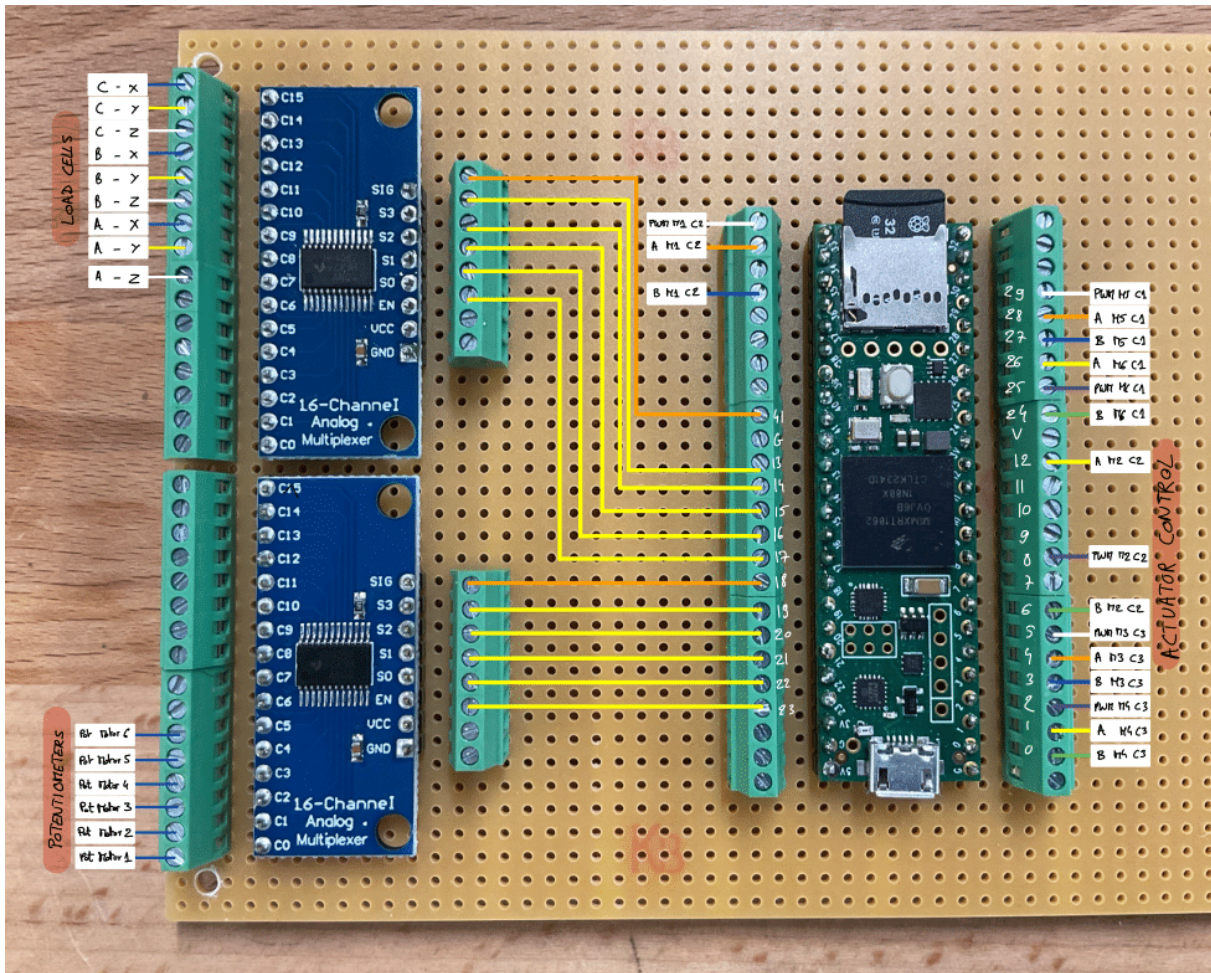


Figure 26: Connections to Teensy 4.1. Notes: "PWM M1 C2" refers to the PWM signal for motor 1 connected to controller number 2, 'A - X' refers to analog input for load cell A (front) axis X, "Pot Motor 1" refers to the potentiometer for motor 1.

Motor	Controller	Output
Motor 1	Controller 2	Motor1 output
Motor 2		Motor2 output
Motor 3	Controller 3	Motor1 output
Motor 4		Motor2 output
Motor 5	Controller 1	Motor1 output
Motor 6		Motor2 output

Table 7: Motor-to-controller output connections.